

---

This is an electronic reprint of the original article.  
This reprint may differ from the original in pagination and typographic detail.

Lahtinen, Katja; Labmayr, Maximilian; Mäkelä, Ville; Jiang, Hua; Lahtinen, Jouko; Yao, Lide; Fedorovskaya, Ekaterina O.; Räsänen, Samuli; Huotari, Simo; Kallio, Tanja

## Long-term cycling behavior of Mg-doped LiCoO<sub>2</sub> materials investigated with the help of laboratory scale X-ray absorption near-edge spectroscopy

*Published in:*  
Materials Today Energy

*DOI:*  
[10.1016/j.mtener.2022.101040](https://doi.org/10.1016/j.mtener.2022.101040)

Published: 01/07/2022

*Document Version*  
Publisher's PDF, also known as Version of record

*Published under the following license:*  
CC BY

*Please cite the original version:*  
Lahtinen, K., Labmayr, M., Mäkelä, V., Jiang, H., Lahtinen, J., Yao, L., Fedorovskaya, E. O., Räsänen, S., Huotari, S., & Kallio, T. (2022). Long-term cycling behavior of Mg-doped LiCoO<sub>2</sub> materials investigated with the help of laboratory scale X-ray absorption near-edge spectroscopy. *Materials Today Energy*, 27, Article 101040. <https://doi.org/10.1016/j.mtener.2022.101040>

---

This material is protected by copyright and other intellectual property rights, and duplication or sale of all or part of any of the repository collections is not permitted, except that material may be duplicated by you for your research use or educational purposes in electronic or print form. You must obtain permission for any other use. Electronic or print copies may not be offered, whether for sale or otherwise to anyone who is not an authorised user.



# Long-term cycling behavior of Mg-doped LiCoO<sub>2</sub> materials investigated with the help of laboratory scale X-ray absorption near-edge spectroscopy



Katja Lahtinen<sup>a</sup>, Maximilian Labmayr<sup>a,b</sup>, Ville Mäkelä<sup>b</sup>, Hua Jiang<sup>c</sup>, Jouko Lahtinen<sup>c</sup>, Lide Yao<sup>c</sup>, Ekaterina O. Fedorovskaya<sup>a</sup>, Samuli Räsänen<sup>d</sup>, Simo Huotari<sup>b</sup>, Tanja Kallio<sup>a,\*</sup>

<sup>a</sup> Department of Chemistry and Materials Science, School of Chemical Engineering, Aalto University, P.O. Box 16100, FI-00076, Aalto, Finland

<sup>b</sup> Department of Physics, University of Helsinki, P.O. Box 64, FI-00014, Finland

<sup>c</sup> Department of Applied Physics, School of Science, Aalto University, P.O. Box 15100, FI-00076, Aalto, Finland

<sup>d</sup> Umicore Finland, B.O. Box 286, FI-67101, Kokkola, Finland

## ARTICLE INFO

### Article history:

Received 27 January 2022

Received in revised form

3 May 2022

Accepted 4 May 2022

Available online 11 May 2022

### Keywords:

Li-ion battery

Doping

Overlithiation

Synthesis

XANES

Valence state

## ABSTRACT

The use of Li-ion batteries is increasing rapidly. Understanding the processes behind active material aging helps to enhance the materials, and therefore, development of new *in situ* methods for structural studies is important. In addition, understanding the effect of different synthesis methods on the active material properties is necessary to optimize the material cycle life. In this work, the performance of LiCoO<sub>2</sub> doped with Mg during the lithiation step is compared to LiCoO<sub>2</sub> prepared using an Mg-doped Co<sub>3</sub>O<sub>4</sub> precursor. *In situ* laboratory-scale X-ray absorption near-edge spectroscopy is used to analyze the Co valence changes in LiCoO<sub>2</sub> to understand the electrochemical behavior of the investigated materials. The maximum reachable Co valence state is found to decrease upon aging, a small decrease indicating a good cycle-life, and this is attributed to the enhanced stacking order, better Mg distribution in the lattice, and fine primary particle size in the material. In the synthesis conditions used in this study, Mg doping during the lithiation step is shown to perform better compared to the precursor doping. Overlithiation is shown to reduce the electrochemical performance of nondoped and precursor-doped LiCoO<sub>2</sub> materials but not to affect the cyclability of lithiation-doped LiCoO<sub>2</sub>.

© 2022 The Author(s). Published by Elsevier Ltd. This is an open access article under the CC BY license (<http://creativecommons.org/licenses/by/4.0/>).

## 1. Introduction

The consumption of Li-ion batteries has been increasing rapidly during the last years due to the increasing demand for consumer electronics and electric vehicles. The annual demand in 2018 was 180 GWh, and the future market is estimated to continue growing 25% annually [1]. The growth threatens to lead to increase in prices and resource shortages of several critical elements for electrode production, such as cobalt and lithium [1–3]. With the increasing demand, it is more important than ever to develop sustainable materials that can endure long use, can be easily recycled, and this way remove pressure from the material producers. For example, as the price and energy needed to produce a battery cell are often high, a long cycle life increases the total energy stored in the system

and lowers the cost and energy spent per energy converted. Long cycle life also increases the time between the changes from old to new cell, decreasing the demand for new materials.

Lithium cobalt oxide (LiCoO<sub>2</sub>, LCO) is the most used positive electrode material in portable digital devices. It has been investigated and used since before the commercialization of Li-ion batteries in 1991, but lately its relative ratio within the positive electrode materials has been reduced due to high price, ethical issues in mining cobalt, and efforts to develop high-energy positive electrodes. LCO is, however, still more stable than many Ni-rich materials and very suitable for portable applications, and thus, it will be most likely used in the future as well. In the past, several different methods, such as stoichiometry modification, particle-size and morphology modification, coating, and doping, have been presented in order to enhance its electrochemical properties [4–6]. Doping has been one of the most popular methods, the typical dopant metals being, for example, Al, Mg, Ti, and Zr [7–11]. The changes induced in LCO depend on the dopant and typically

\* Corresponding author.

E-mail address: [tanja.kallio@aalto.fi](mailto:tanja.kallio@aalto.fi) (T. Kallio).

include crystal structure stabilization [12,13], reduced positive electrode dissolution [4], enhanced conductivity and Li diffusion through changes in the crystal structure [4,7,14], and changes in morphology [15,16]. Double doping [7,12,17] and combination of doping and coating [18,19] have also been investigated lately. Finally, adding excess Li has been investigated as well while aspiring to increase the specific capacity of the active material and reduce the effect of irreversible Li loss during cell formation [20,21].

There are several ways to add the dopant in the electrode material. The most popular one in the literature has been so-called lithiation doping, in which the dopant is mixed to the material simultaneously when the Li precursor is added to the  $\text{Co}_3\text{O}_4$  precursor. An alternative for this method is precursor doping, in which the dopant is added to the Co precursor before the lithiation step. Both methods are used in the industry, but there seems to be no clear understanding, which one improves the battery active material properties more effectively. Therefore, it is interesting that while countless studies on the doping methods have been done, the lithiation and precursor doping have not been compared before. Thus, the goal of this work is to investigate how the doping step affects the electrochemical performance of LCO and to understand what causes the differences between the differently synthesized materials. Mg has been selected for this work because its use as a dopant for LCO is quite established, and while it is electrochemically inactive in Li-ion (de-)intercalation, it is known to enhance electrochemical performance of LCO in small amounts when added with conventional doping methods [12,18] (list of publications related to Mg doping of LCO can be found in Supporting Information). Recently, the research on Mg-doped LCO has focused on improving the high-voltage (<4.5 V) stability of the material [9,10,18]. However, here the focus is in understanding the doping stage differences, and hence, a commercial cut-off voltage of 4.4 V is used. The improvements caused by Mg are usually attributed to improved structural stability or conductivity [12], which can increase the cycle life of the material. The doping methods are tested in both stoichiometric and overlithiated Li/Co stoichiometries to investigate whether the doping method is dependent on the LCO stoichiometry.

When material cycle life is investigated, it is important to be able to understand the processes occurring in the cells during the long-term cycling. For this, *in situ* and *operando* setups to measure the cells with existing techniques have been developed during the last 10 years. *In situ* setups have been presented for several different techniques such as scanning electron microscopy (SEM) [22], transmission electron microscopy (TEM) [23], neutron diffraction [24], Raman spectroscopy [25], X-ray diffraction (XRD) [26], X-ray absorption spectroscopy (XAS) [27], transmission X-ray microscopy [28], and many others. Compared to samples measured *ex situ*, *in situ/operando* measurements have several advantages. First, the sample preparation steps are reduced; second, the risk of sample contamination and side reactions due to the exposure to, for example, humidity are lowered; third, the nonequilibrium and fast-transient processes can be investigated [29,30]. The signal of *in situ/operando* methods is often limited to small area, and the cell design can be complicated, and thus, *ex situ* measurements are necessary too. However, in measuring the processes occurring in the cell, *in situ/operando* methods are advantageous.

XAS is an element specific probe of the local electronic and geometric structure around the absorbing atom or ion [31]. It can be roughly divided into two classes: X-ray absorption near-edge structure (XANES) and extended X-ray absorption spectroscopy fine structure (EXAFS), which in principle are parts of the same spectra but are usually treated differently. XANES can give information on the oxidation state and the local symmetry around the absorbing ion or atom, while EXAFS reveals coordination numbers

and the coordination shells' distances as well as disorder. Since the 1970s and advent of synchrotron light sources, XAS has been a technique nearly exclusively available at synchrotrons. However, accessing synchrotron is challenging, as the application periods are long, and the time slots given relatively short. Therefore, monitoring electrode materials at different states of charge (SOCs) or states of health (SOHs) is in practice not feasible. In the recent years, however, thanks to the advancement of X-ray crystal optics, high-resolution XANES can be performed also in a laboratory-scale setting with conventional X-ray tubes [32–34]. The penetrating nature of hard X-rays enables nondestructive XAS studies at the 3d transition metal K edges (for Co K edge, photon energy is 7.1 keV). The method can thus be used to probe cells in normal *operando* conditions. While the laboratory-scale XANES technique has several advantages, it has not yet been utilized to battery research to a large extent. Currently only a few investigations on  $\text{LiNi}_x\text{Co}_y\text{Mn}_{1-x-y}\text{O}_2$  materials have been published [35,36]. In this work, we show that  $\text{LiCoO}_2$ /graphite pouch cells can be measured with this method *in situ* without utilizing the limited time slots available in synchrotrons. The purpose of the work is to understand does the differently added Mg doping affect the valence state of cobalt during  $\text{LiCoO}_2$  aging, and how it is reflected in the electrochemical performance. To the knowledge of the authors, this is the first time a laboratory-scale XANES is used to investigate  $\text{LiCoO}_2$  in a pouch cell setup.

## 2. Experimental

Six different LCOs synthesized *via* a solid-state method were investigated in this work. The samples are denoted as s-LCO, s-L-LCO, s-P-LCO, o-LCO, o-L-LCO, and o-P-LCO referring to a stoichiometric LCO, lithiation step Mg-doped LCO, precursor Mg-doped LCO, overlithiated LCO, overlithiated lithiation step Mg-doped LCO, and overlithiated precursor Mg-doped LCO, respectively. The precursors and investigated LCOs were provided by Umicore Finland. The sample compositions are collected in Table 1. Mg-doped  $\text{Co}_3\text{O}_4$  and plain  $\text{Co}_3\text{O}_4$  were synthesized by firing Mg-doped  $\text{Co}_2(\text{OH})_2\text{CO}_3$  and plain  $\text{Co}_2(\text{OH})_2\text{CO}_3$  in air, respectively. The LCOs were synthesized *via* the solid-state synthesis at 1020 °C in a muffle furnace (Carbolite, CWF1200) using  $\text{Co}_3\text{O}_4$  or Mg-doped  $\text{Co}_3\text{O}_4$  and  $\text{Li}_2\text{CO}_3$  as precursors and  $\text{Mg}(\text{OH})_2$  for doping during the lithiation step. The Li/Co ratio for the  $\text{Li}_2\text{CO}_3$  and  $\text{Co}_3\text{O}_4$  precursors was 1.005 for stoichiometric LCOs and 1.050 for overlithiated LCOs during the synthesis.

The synthesis products were analyzed using inductively coupled plasma optical emission spectrometer (ICP-OES, Thermo Scientific iCAP6500). After this, the crystal structures were characterized with XRD using a PANalytical X'Pert Pro Alpha-1 diffractometer (Cu  $K_{\alpha 1}$ -radiation). The  $2\theta$  range was 10–90°, the step size 0.013°, the scan speed 0.2°/min, and the pulse height discrimination (PHD) range 44–100%. The morphology and size of the particles was investigated by means of SEM (Tescan Mira-3) with in-beam secondary electrons and accelerating voltage of 5 kV. The samples were coated with 80/20 Au/Pd by sputtering to ensure the conductivity of the samples during the imaging. To investigate the valence states of the elements in LCOs, electron energy loss spectroscopy (EELS) measurements were performed. A double aberration corrected JEOL JEM-2200FS microscope equipped with a 200 kV field-emission gun (FEG) and an in-column energy filter (Omega filter) was used for this. Focused ion milling (FIB, JEOL JIB 4700 F Multi Beam System) was used to cut the particles for the EELS measurements. Prior to the FIB milling, a 1  $\mu\text{m}$  thick Pt protective layer was coated on the target particle by ion beam deposition inside the FIB. The final lamellas were approximately 50 nm thick. Raman spectrometer (Renishaw, inVia confocal Raman

**Table 1**  
Nominal composition of the investigated LCO materials based on ICP-OES.

	Doping type	Li/Co ratio, nominal	Li/Co ratio, product	Sample composition
s-LCO	–	1.005	1.01	Li <sub>1.005</sub> Co <sub>0.995</sub> O <sub>2</sub>
s-L-LCO	lithiation	1.005	1.03	Li <sub>1.014</sub> Co <sub>0.981</sub> Mg <sub>0.005</sub> O <sub>2</sub>
s-P-LCO	precursor	1.005	1.02	Li <sub>1.006</sub> Co <sub>0.988</sub> Mg <sub>0.006</sub> O <sub>2</sub>
o-LCO	–	1.050	1.04	Li <sub>1.019</sub> Co <sub>0.981</sub> O <sub>2</sub>
o-L-LCO	lithiation	1.050	1.05	Li <sub>1.021</sub> Co <sub>0.974</sub> Mg <sub>0.005</sub> O <sub>2</sub>
o-P-LCO	precursor	1.050	1.04	Li <sub>1.016</sub> Co <sub>0.978</sub> Mg <sub>0.006</sub> O <sub>2</sub>

microscope) with a 532 nm argon ion laser as the source of excitation in the range of 80–1200 cm<sup>-1</sup> (spot size ~721 nm, number of scans/measurement 10) was used to analyze the vibration characteristics of the samples. X-ray photoelectron spectroscopy (XPS) measurements were made using Kratos Axis Ultra system, equipped with a monochromatic Al K $\alpha$  X-ray source. All measurements were performed with 0.3 mm  $\times$  0.7 mm analysis area and the charge neutraliser on. The wide scans were performed with 80 eV pass energy and 1 eV energy step and the high-resolution scans with 20 eV pass energy, 0.1 eV steps size. The energy calibration was made using the adventitious carbon C 1s component at 284.8 eV (Supporting information Fig. S1).

The electrodes for the electrochemical tests were prepared in the following way. The electrode consisted of 95 wt-% active material, 2 wt-% conductive carbon (Timcal Super C65), and 3 wt-% polyvinylidene fluoride (PVDF, Solvay Solef 5130). N-methyl-2-pyrrolidone (NMP, BASF Life Science) was used as a solvent with a solvent content in the slurries being 40 wt-%. The slurries were mixed with a dispergator (Dispermat, VMA-Getzmann GMBH-D-51580 Reichshof) using 500 rpm. The homogeneous electrode slurries were then coated on an aluminum foil with a wet thickness of 120–130  $\mu$ m to obtain a loading of 7.5–8.0 mg/cm<sup>2</sup>. The coatings were dried in a fume hood overnight and then in 80 °C oven for 4 h. After this, electrodes with 14 mm diameter were cut and then calendared using a pressure of 1950 kg/cm<sup>2</sup>. To assemble the electrodes to cells in an argon-filled glovebox (Jacomex, c<sub>O2</sub><0.3 ppm, c<sub>H2O</sub> < 0.3 ppm), they were dried under vacuum at 110 °C overnight before transferring to the glovebox.

The cell assembly for electrochemical tests was done fully in the glovebox. For half-cell measurements, Hohsen 2016 cases were used. A 0.75 mm thick lithium metal foil (Alfa Aesar) was used as a counter electrode and 1 M lithium hexafluorophosphate (LiPF<sub>6</sub>) dissolved in 1:1 ethylene carbonate (EC):dimethyl carbonate (DMC) solution (BASF, LP30) as an electrolyte. A Whatman GF/A 0.26 mm thick glass fiber filter was used as a separator and MTI 0.2 mm stainless steel spacers to fill the extra space in the cell. The cells were stabilized for 24 h before beginning the testing. The three-electrode measurements were conducted in commercial EL-Cell test cells. Lithium metal served both as the counter and reference electrode. 1 M LiPF<sub>6</sub> in 1:1 EC:DMC was used as the electrolyte and a 1.55 mm thick glass fiber separator (EL-Cell) to separate the electrodes. Similarly to the half-cell measurements, the cell was stabilized for 24 h before the testing. In the pouch cells for long-term cycling, graphite (Hitachi) was used as the negative electrode and the investigated LCOs as the positive electrode. The graphite slurry contained 92 wt-% graphite, 4 wt-% conductive carbon, and 4 wt-% PVDF (Kureha). Copper foil was used as a current collector for the electrode with the graphite loading being 5.3–6.5 mg/cm<sup>2</sup>. The LCO slurry had the same composition as in the half-cells except for a slightly higher loading, 12–14 mg/cm<sup>2</sup>. The cells contained one positive-negative electrode pair. 1 M LiPF<sub>6</sub> in 25:70:5 EC:diethylene carbonate (DEC):propylene carbonate (PC) solution with 1 mol% vinylene carbonate (VC) and 1 mol% 1,3-propane sultone (PS) doping (Golden Light Hi-Tech Energy Storage Materials, JR-02) was used as an electrolyte in the pouch cells.

Cyclic voltammetry (CV) and rate capability tests were performed in half-cells. CVs of the materials were investigated in the voltage range of 3.0–4.4 V and scan rate of 0.02 mV/s using a Biologic potentiostat (MGP-205). The galvanostatic rate capability measurements were performed using a Neware battery cycler in the same voltage range. The formation C-rate was 0.03 C, after which the actual measurement was done. The discharge C-rates used in the program varied between 0.1 C and 4.0 C, while the charge C-rate was kept constant at 0.2 C. At least three parallel samples were measured to ensure the repeatability of the results. The pouch cell aging was done with the Neware cycler as well using a voltage range of 3.0–4.3 V and the C-rate of 0.5 C. The cells were cycled to 1000 cycles or to SOH of 80%, whichever was reached first.

While the EELS L-edge measurements reveal transitions from the 2p shell to the unoccupied 3 d states, the Co K-edge XANES studies transitions from the 1s to the unoccupied states of mostly 4p in character. The Co K-edge XANES measurements were performed using a laboratory-scale X-ray absorption spectrometer (Center for X-ray Spectroscopy, Department of Physics, University of Helsinki) [34]. The spectrometer was wavelength dispersive and based on the Johann geometry. In the experiment a Si(533) strip-bent monochromator (radius of curvature R = 0.5 m) [37] was used. The energy resolution was estimated to be 2 eV. The spectra were measured between 7.62 and 7.84 keV with an energy step size of 1 eV in the pre-edge background and post-edge regions, and with an energy step of 0.5 eV in the near-edge region. Additional information on the data processing is collected in Supporting information. Electrochemical impedance spectroscopy (EIS) measurements were performed with an Autolab potentiostat (PGSTAT302 N) using an FRA software. The frequency range of 10 mHz–100 kHz and alternating potential amplitude of 5 mV were used. The measurements were done at the open circuit voltage (OCV) corresponding to the SOC of 50%.

### 3. Results and discussion

#### 3.1. Characterization of the materials

The chemical composition, structure, and morphology of LCOs were investigated with ICP-OES, XRD, EELS, Raman spectroscopy, XPS and SEM. The ICP-OES results are presented in Table 1 and the elemental analysis shows that the Li/Co ratio of the materials varies slightly from the synthesis parameters. However, as the Li/Co ratio for the over-lithiated samples is always larger than for the stoichiometric samples, the comparison between two different lithium contents can be made.

The XRD results of the investigated materials are presented in Fig. 1a, and they show that all the samples have well-defined crystalline rhombohedral structure of LiCoO<sub>2</sub> with hexagonal setting. The material compositions were analyzed using the LeBail method and the program Fullprof [38], and the obtained lattice parameters are presented in Table 2. The reliability factor values for the weighted profiles ( $R_{wp}$ ) are between 10 and 13% and the expected reliability factor ( $R_e$ ) for the data is 3–8%. The lattice parameter  $a$  is observed to be relatively similar for all samples with the variation being between 2.816 and 2.817 Å. In the lattice

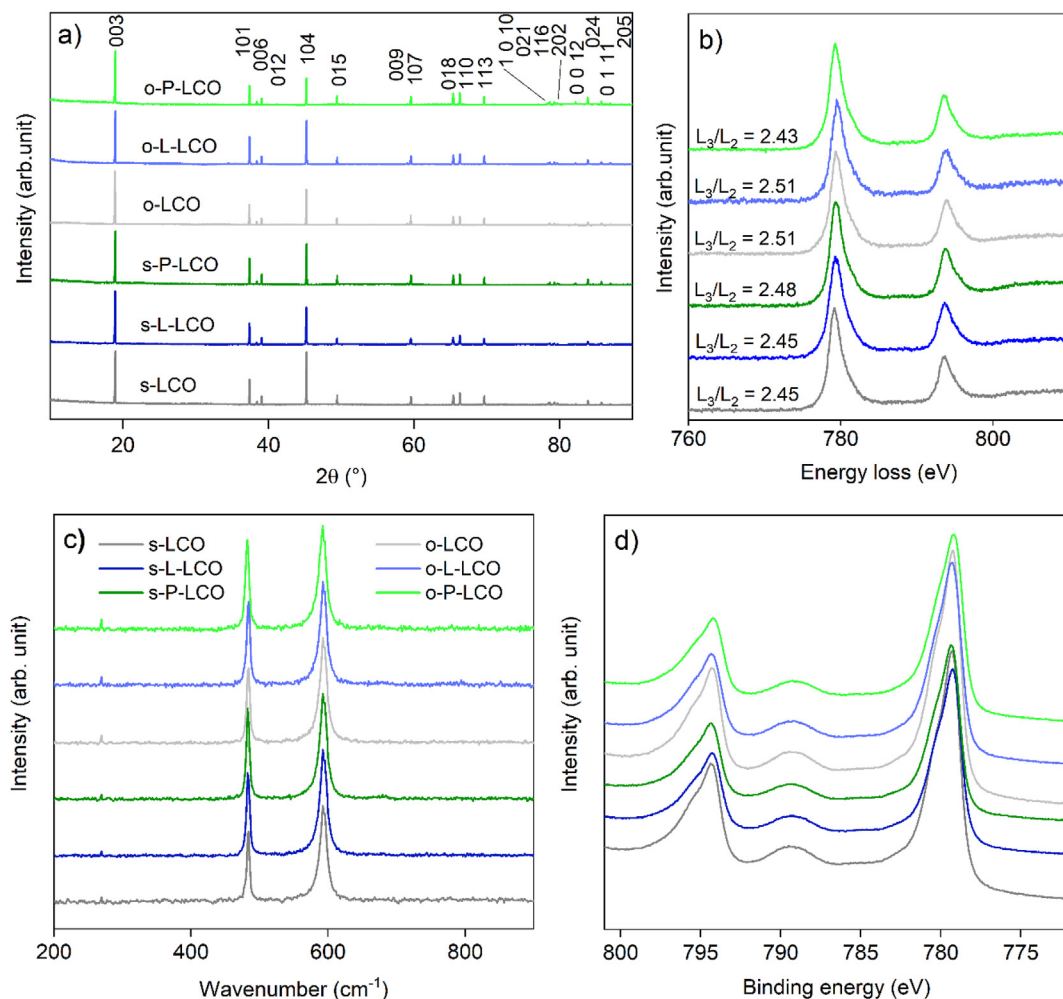


**Fig. 1.** Structural data of the investigated LCOs. a) XRD spectra, b) EELS spectra of cobalt L-edge and the calculated  $L_3/L_2$  ratios, c) Raman spectra, d) XPS spectra of cobalt 2p spectra. The color coding is the same in all images followingly; dark grey: s-LCO, dark blue: s-L-LCO, dark green: s-P-LCO, light grey: o-LCO, light blue: o-L-LCO, light green: o-P-LCO.

parameter  $c$ , on the other hand, differences are observed. s-LCO and o-LCO have the same  $c$  parameter, 14.053 Å, indicating that the over-lithiation does not affect the crystal structure. The Mg doping, however, increases the lattice parameter  $c$ . s-L-LCO and o-L-LCO have the highest  $c$  parameters, 14.059 Å for both. s-P-LCO and o-P-LCO have lower values than those, 14.055 Å and 14.056 Å, respectively, but yet higher than the non-doped samples. This indicates that the lithiation step doping affects the crystal structure more than the precursor step doping. The increase in the  $c$  parameter is attributed to the larger ionic radii of  $Mg^{2+}$  (0.72 Å) compared to the low-spin  $Co^{3+}$  (0.55 Å) [39] as Mg typically replaces Co in the LCO lattice structure.

**Table 2**

Selected structural parameters of the investigated LCO samples extracted from the LeBail fittings.

Sample	$a$ (Å)	$c$ (Å)	$(I_{012}+I_{006})/I_{101}$
s-LCO	$2.81608 \pm 0.00005$	$14.0529 \pm 0.0002$	0.52
s-L-LCO	$2.81619 \pm 0.00005$	$14.0611 \pm 0.0002$	0.51
s-P-LCO	$2.81628 \pm 0.00005$	$14.0569 \pm 0.0002$	0.57
o-LCO	$2.81620 \pm 0.00005$	$14.0531 \pm 0.0002$	0.57
o-L-LCO	$2.81675 \pm 0.00005$	$14.0592 \pm 0.0002$	0.49
o-P-LCO	$2.81693 \pm 0.00008$	$14.0561 \pm 0.0003$	0.58

Space group  $R\bar{3}m$  (#166), hexagonal setting.

To verify the Mg distribution in the lattice, local disorder of the cations was studied within the limits of XRD scattering resolution. While Mg typically replaces Co, it could also replace Li as their size and charge density are similar. Previously Mladenov et al. [40] have shown that the larger the percentage of Mg in the Co site is, the larger the  $c$  parameter is. On the other hand, a low synthesis temperature has been reported to increase the amount of Mg in the Li site. Due to small concentration of Mg in the samples, the occupancies of Li, Mg and Co could not be freely refined. However, the Mg occupancy was tested by manually testing different percentages of it at Co and Li sites, and based on that all Mg is located on the Co site in all the samples. The difference in  $R_{Bragg}$  to all Mg in the Li site is 1.3% for the stoichiometric samples and only 0.3% for the over-lithiated ones, which indicates that the results are not the most reliable statistically. As all Mg is located in the Co sites, this does not explain the differences in the  $c$  parameter. Instead, the difference is plausibly caused by Mg distribution in the samples, which is discussed in context of the XPS results below.

The intensity ratio of the Bragg reflections  $(I_{012}+I_{006})/I_{101}$  of the samples were calculated to understand the crystal structures of the materials better. This intensity ratio is related to the level of hexagonal stacking order [41], an increasing value indicating decreasing order. The calculated values are collected in Table 2. While the differences between materials are quite small, the results

suggest that the stacking order is slightly better for s-LCO, s-L-LCO and o-L-LCO, which indicates that doping at the lithiation step provides particles with a well-ordered crystal structure. The improvement is especially good for the over-lithiated sample. On the other hand, for the non-doped samples over-lithiation increases the stacking disorder in the structure.

EELS was measured to obtain information about the valence state of cobalt in the investigated LCOs as the L edge of cobalt is sensitive to it [42,43]. The  $L_3$  and  $L_2$  edges are induced by the electron transitions from the 2p orbitals to the unoccupied 3d orbitals. To measure EELS, the LCO particles were cut with the FIB. The images of the cut particles are collected in Supporting information, Fig. S2 and the EELS measurement positions in Fig. S3. The EELS results collected in Fig. 1b show that the  $L_3$  and  $L_2$  edge positions are very similar for all the samples, being 779.4–779.8 eV and 793.8–794.0 eV, respectively. To confirm the valence states, the  $L_3/L_2$ -edge intensity ratios of the LCOs were calculated using a method presented by Wang et al. [43], and the results are collected in Fig. 1b. The ratio is related to the unoccupied states of the 3d orbital and therefore provides information on the valence states, as its value varies from 2 to 5 for the valence states of 4+ and 2+, respectively [42,43]. In our study, the  $L_3/L_2$  intensity ratios are 2.43–2.51 for the investigated active materials, showing only minor variation. These results together with the energy loss peak determination thus indicate that there are no notable differences in the valence states of cobalt in the investigated materials. This is a logical result, as the Mg concentration in the samples is small (Table 1).

The Raman spectroscopy results collected in Fig. 1c show the characteristic modes of  $e_g$  and  $a_{1g}$  for hexagonal  $\text{LiCoO}_2$  at  $485\text{ cm}^{-1}$  and  $595\text{ cm}^{-1}$ , respectively, for all the investigated LCOs. The  $e_g$  band is attributed to O–Co–O bending and  $a_{1g}$  band to Co–O stretching vibrations [44]. In addition, a low intensity extra band at  $680\text{ cm}^{-1}$  is observed for s-P-LCO (Fig. S4 in Supporting information) and this is attributed to either cubic spinell ( $Fd-3m$ ) phase or  $\text{Co}_3\text{O}_4$ . As  $\text{Co}_3\text{O}_4$  is used as a precursor in the synthesis, its presence in the samples is plausible even though it is not observed in the XRD measurements (Fig. 1a). With Raman spectroscopy, the LCO particles can only be observed up to 100 nm depth based on the penetration depth of green laser while the whole sample can be observed with XRD [45]. As the presence of compounds on the surface is amplified in Raman, it is possible that unreacted  $\text{Co}_3\text{O}_4$  traces exist in the surface of s-P-LCO and that its amount is too small to be detected with XRD but large enough for Raman. The  $\text{Co}_3\text{O}_4$  band appears only for the precursor-doped LCO but not for the lithiation-doped LCO, which suggests that the lithiation process for the lithiation-doped LCO is more complete. This is in agreement with the  $(I_{012}+I_{006})/I_{101}$  values collected in Table 2 which show that the lithiation-doped samples are more ordered compared to the precursor-doped ones. As the lithiation step is the same for the materials, except introducing the dopant already added to the s-P-LCO precursor, adding the dopant during the last synthesis step might also enhance the lithiation process or prevent the Li evaporation. The  $\text{Co}_3\text{O}_4$  band is not observed in the over-lithiated LCOs, which can be attributed to the larger amount of lithium available during the synthesis, and therefore the  $680\text{ cm}^{-1}$  band is concluded to be caused by unreacted  $\text{Co}_3\text{O}_4$ .

The surface composition of the samples was further studied by XPS to investigate the material composition at the very surface (depth of app. 10 atom layers) of the particles. The Co 2p spectra of the LCOs are shown in Fig. 1d and they correspond well to previously reported Co 2p spectra of  $\text{LiCoO}_2$  [46] or  $\text{Co}_3\text{O}_4$  [47]. The differentiation between  $\text{Co}_3\text{O}_4$  and  $\text{LiCoO}_2$  is difficult as Co 2p for  $\text{Co}^{3+}$  and  $\text{Co}^{2+}$  are very close to each other. The shape of the Co 2p region is known to be a better indication on the chemical state than

the bare position of the peak maximum [48], and as only minor differences can be observed in the spectra, no notable conclusions can be drawn from them.

The concentration data obtained from the XPS results is collected in Table 3 and when comparing to the ICP-OES data (Table 1), Mg appears to be enriched in the surface of all the samples. Higher Mg concentrations in s-L-LCO (2.0%) and s-P-LCO (7.1%) are detected when compared to o-L-LCO (0.5%) and o-P-LCO (1.1%). Interestingly, the surface Mg concentration is larger in the precursor-doped sample than in the lithiation-doped materials. As the dopant is added simultaneously with the Li precursor for the lithiation-doped sample, it could be expected to locate closer the surface region. However, based on the results, it seems that the Mg dopant is diffused into the lattice better in the lithiation-doped than precursor-doped sample. This is also supported by the XRD results, which show that the increase in the lattice parameter  $c$  caused by Mg insertion is larger for the lithiation-doped samples than for the precursor-doped ones. The Mg concentrations on the surface are smaller in the over-lithiated samples, indicating that the excess Li might enhance the Mg immersion in the structure.

To observe if there are differences in the element content of the sample surfaces between the stoichiometric and over-lithiated samples, the Li/Co, O/Co, and Mg/Co ratios obtained from the XPS measurement were calculated and collected in Table 3. Two observations are made. First, the value of the Li/Co ratio (0.4–0.8) is clearly lower than expected 1 from the stoichiometry of  $\text{LiCoO}_2$ . Second, the O/Co ratio is larger than the expected value. The second point is understandable as oxygen containing molecules are always absorbed from the atmosphere to the sample surfaces and XPS detects them which results as an apparently higher oxygen concentration. As the XRD measurement shows that the bulk material corresponded well to  $\text{LiCoO}_2$  with expected Li content, the XPS data indicates that there is a thin lithium-poor layer on the surface of all the materials. As the Raman results show  $\text{Co}_3\text{O}_4$  band for only s-P-LCO, the lithium-poor layer is most likely thickest for this sample. The smallest Li/Co ratio of s-P-LCO (0.4) also supports this.

The morphology of the LCO materials was investigated with SEM, and the micrographs are presented in Fig. 2. The micrographs of  $\text{Co}_3\text{O}_4$  and Mg-doped  $\text{Co}_3\text{O}_4$  precursors can be found in Supporting information Fig. S5. The particles are observed to be spherical with the average size of  $17.6\text{ }\mu\text{m}$  in diameter and consist of clustered primary particles. The size and shape of the primary particles varies between the samples. The smallest primary particles are observed for s-L-LCO and o-L-LCO which have the typical particle size between 2 and  $3\text{ }\mu\text{m}$ . The non-doped and precursor-doped samples have quite a similar primary structure, with the primary particles typically being rectangle-shaped, the height and width varying between 2 and  $10\text{ }\mu\text{m}$ . This result indicates that the particle morphology is affected by the method of doping. As the lithiation step doping produces particles with finer morphology compared to the non-doped and precursor-doped samples, the dopant added during the lithiation step can be concluded to cause the difference. Recently, Hong et al. [16] showed that even a small

**Table 3**  
Element concentrations on the surfaces of the investigated LCOs determined with XPS. Carbon is omitted in the concentration analysis as a clear contaminant due to the sample transfer.

	Co 2p (%)	O 1s (%)	Li 1s (%)	Mg 2p (%)	O/Co	Li/Co	Mg/Co
s-LCO	24	63	13	–	2.2	0.8	–
s-L-LCO	23	61	14	2.0	2.6	0.8	0.09
s-P-LCO	24	61	7.4	7.2	2.8	0.4	0.30
o-LCO	27	60	13	–	2.1	0.7	–
o-L-LCO	26	61	12	0.5	2.2	0.8	0.03
o-P-LCO	27	61	11	1.1	2.2	0.5	0.04

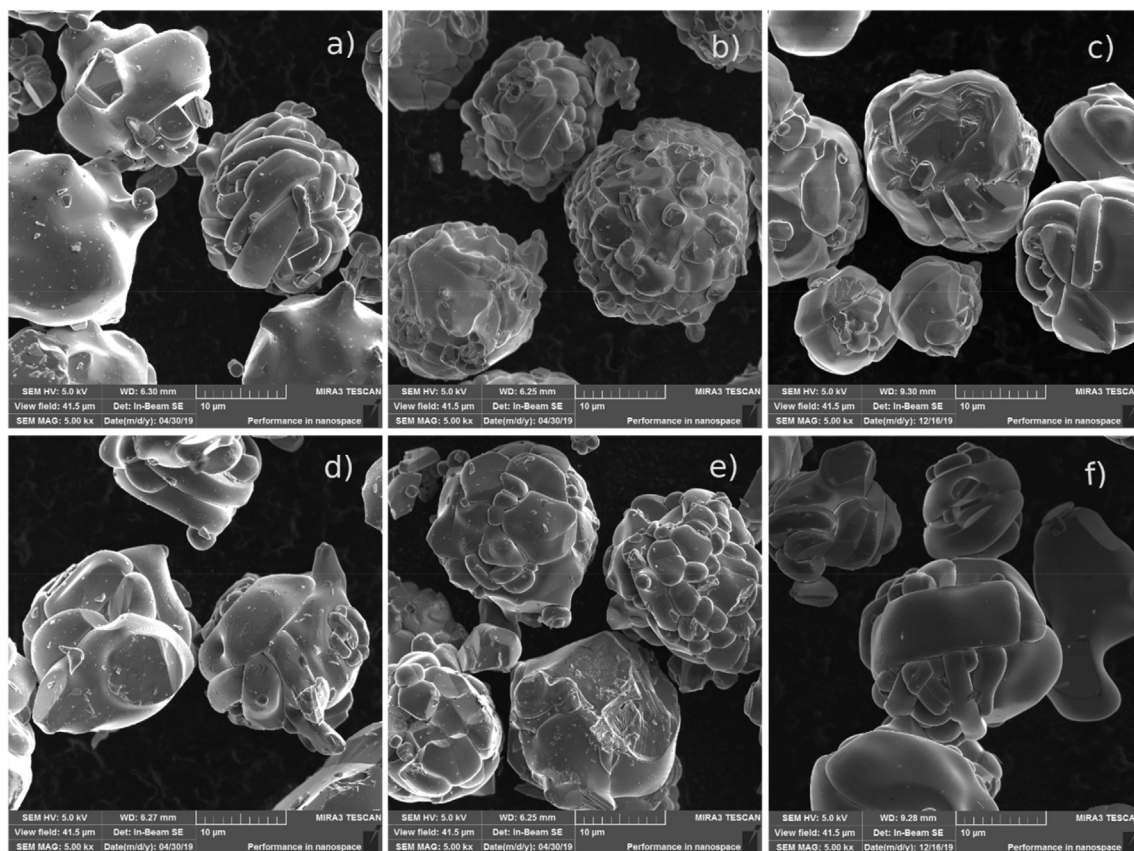


**Fig. 2.** SEM images of the a) s-LCO, b) s-L-LCO, c) s-P-LCO, d) o-LCO, e) o-L-LCO, f) o-P-LCO powders.

amount of doping induces lattice distortions in the core material which leads to robust surface morphology. While the XRD data (Table 2) shows that the lithiation-doped samples are well-ordered, it is possible that the dopant affects the morphology on the particle surface in a layer so thin that it is not observed with XRD. The cross-section images of the samples collected in Supporting information Fig. S2 support this hypothesis as the bulk of the materials is observed to be relatively uniform for all samples. In the precursor-doped and non-doped samples there are no additional components mixed with the Co and Li precursors, which therefore causes similar morphologies for the materials synthesized *via* this method, even if the precursor morphology is slightly different, as seen in Fig. S5. To summarize the results from the structural characterization, as well as to facilitate the connecting of different results, a schematic concluding the results is presented in Supporting Information in Fig. S8.

### 3.2. Electrochemical characterization of the LCOs

The electrochemical behavior of the studied LCOs was investigated using CV, and the voltammograms obtained after the formation are presented in Fig. 3. Three peaks are observed during both the Li insertion and extraction scans for all the materials. The largest peak is caused by Li deintercalation/intercalation reaction in the two-phase domain [49], and the position of the peak varies depending on the material, being 3.957 V/3.875 V, 3.967 V/3.876 V and 3.986 V/3.853 V for s-LCO, s-L-LCO and s-P-LCO, respectively, and 3.964 V/3.874 V, 3.957 V/3.879 V and 3.993 V/3.850 V for o-LCO, o-L-LCO and o-P-LCO, respectively. The first value indicates the Li extraction voltage and the second value the Li insertion voltage. If the stoichiometric LCOs are compared, the peak separation can be

observed to be the smallest for s-LCO, and the largest for s-P-LCO. For the over-lithiated samples, o-L-LCO has the smallest peak separation and o-P-LCO the largest. If the stoichiometric samples are compared to their corresponding over-lithiated counterpart, the former have a smaller peak separation in case of the non-doped and precursor-doped samples. For the lithiation-doped samples, the over-lithiated one shows a slightly smaller peak separation. The larger the peak separation is, the more irreversible the reaction is [50]. Therefore, the precursor-doped samples, s-P-LCO and o-P-LCO, can be concluded to have the most irreversible behavior among the studied materials. For the non-doped materials, the over-lithiation seems to render the material slightly more irreversible. In contrast, for the lithiation-doped materials, the over-lithiation seems to make the material more reversible.

The peak intensity can also be observed to vary between the samples, which indicates that there are differences in the electrode kinetics [51]. For the stoichiometric samples, the Mg doping seems to lower the maximum intensity and increase the peak width, with the s-L-LCO peaks being sharper than the s-P-LCO peaks. For the over-lithiated samples, o-LCO and o-L-LCO have similar peak intensities while o-P-LCO has clearly smaller than the other two. This suggests that the precursor doping increases the resistance of the LCO compared to the lithiation doping. For the stoichiometric materials, also the lithiation doping seems to increase the LCO resistance, but for over-lithiated LCO the lithiation doping does not appear to affect it.

The rate capability was investigated to further understand the electrochemical properties of the LCO materials. The voltage range of 3.0–4.4 V in the half cells was selected to offer a commercially relevant voltage range. The results presented in Fig. 3c show that the initial capacities of the materials obtained at the C-rate of 0.03 C

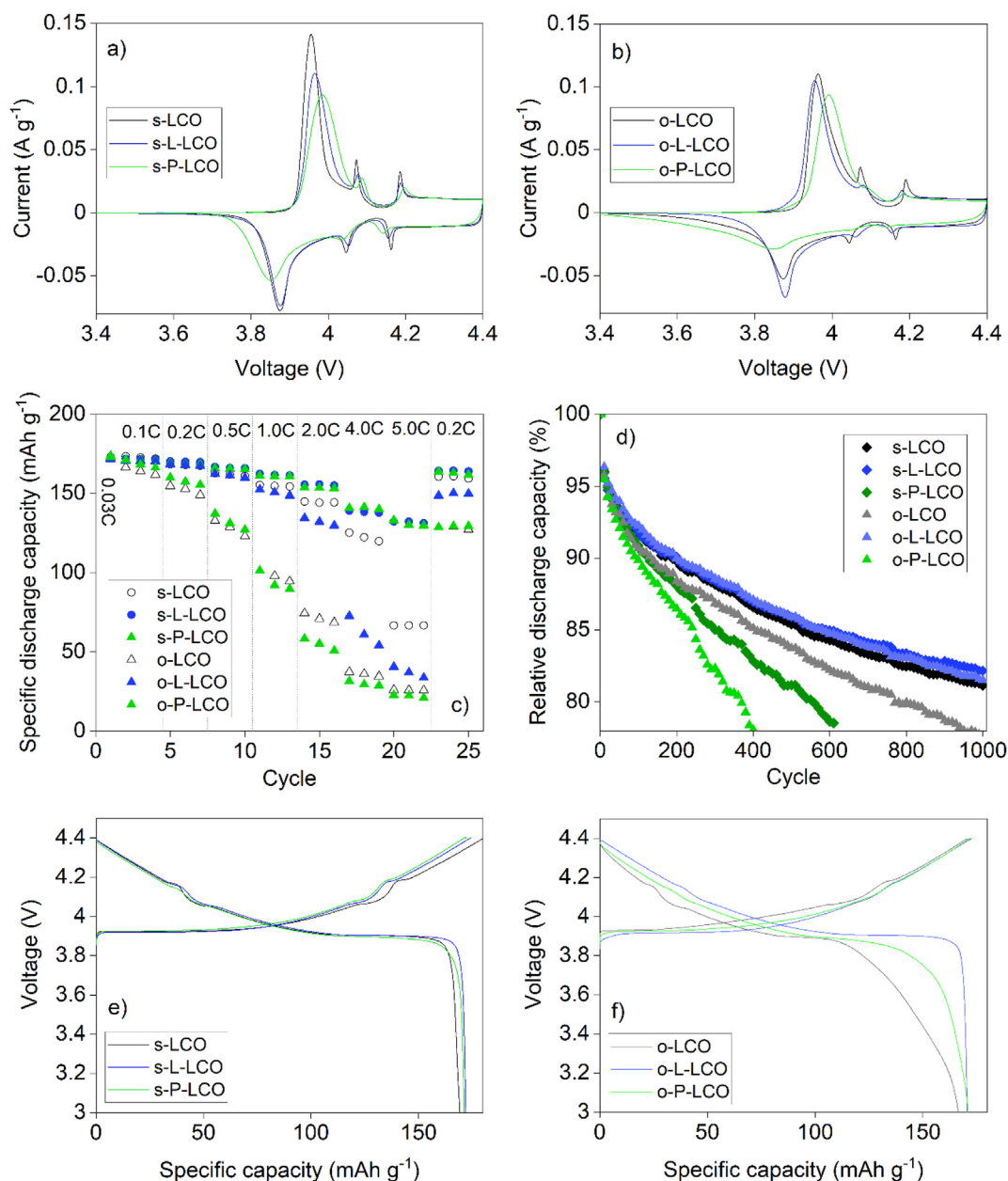


**Fig. 3.** Electrochemical results of the investigated LCOs. a) Cyclic voltammograms of the stoichiometric LCOs at scan rate of 0.02 mV/s<sup>1</sup>, b) cyclic voltammograms of the over-lithiated LCOs at scan rate of 0.02 mV/s<sup>1</sup>, c) rate capability properties of the investigated materials in the voltage range of 3.0–4.4 V (half-cells), d) cycling performance of the LCO/graphite pouch cells in the voltage range of 3.0–4.3 V and the C-rate of 0.5 C, e) charge-discharge curves of the stoichiometric LCOs at 0.1 C and f) charge-discharge curves of the over-lithiated LCOs at 0.1 C.

are similar to the integrated peak areas reported in the CV results with the average value approximately 173 mAh/g and no notable variation between the materials. However, as the discharge current is increased, variations can be observed. Already at 0.2 C current, o-LCO and o-P-LCO can be seen to have lower discharge capacity than the other samples. The difference to the best performing s-L-LCO and s-P-LCO increases with every C-rate, until at 5.0 C the capacity of o-LCO and o-P-LCO is only around 25 mAh/g while for s-L-LCO and s-P-LCO it is around 130 mAh/g. The two other samples, s-LCO and o-L-LCO have the rate capability between these two. Up to 1.0 C the capacity of both the materials stays high, around 150 mAh/g, but after that at higher C-rates the decrease is larger. The discharge capacities at 5.0 C for these materials are 67 mAh/g and 37 mAh/g, for s-LCO and o-L-LCO, respectively. The results clearly show that

the Mg doping regardless of the doping method enhances the rate capability of the stoichiometric LCO. For the over-lithiated materials, the Mg doping introduced at the lithiation step seems to improve the performance slightly, but the precursor doping does not affect the properties. The difference between the precursor and lithiation-stage doping is most likely caused by the differences observed in the particle morphologies in Fig. 2. The finer primary particle size of the lithiation-doped material enhances the Li-ion insertion to the material and thus enhances the capacity compared to the precursor-doped materials. Previously, Mg doping has been shown to enhance LCO conductivity and thus the overall performance [52]. In our results, Mg enhances the performance in three cases out of four. This indicates that while adding Mg can indeed enhance the LCO performance, the doping method affects

the properties of the sample, e.g. the morphology, and should be taken into consideration while performing the synthesis and comparing the results reported in literature.

Initial information about the capacity retention of the materials can be obtained by comparing the 0.2 C capacity at the end of the rate capability measurement to the initial 0.2 C capacity. The smaller the drop from the initial 0.2 C to the end 0.2 C is, the better cyclability this indicates. Based on Fig. 3c, the stoichiometric LCOs have a clearly better capacity retention than the over-lithiated LCOs. Of the over-lithiated samples, o-L-LCO shows better capacity retention than the other two samples. However, to verify these observations, long-term cycling has been carried out in pouch cells.

The long-term cyclability of the studied materials was investigated by cycling them in LCO/graphite pouch cells in the voltage range of 3.0–4.3 V. The results collected in Fig. 3d show that s-LCO, s-L-LCO and o-L-LCO all reach 1000 cycles without the relative discharge capacity decreasing below SOH 80%. o-LCO, s-P-LCO and o-P-LCO on the other hand, have a poorer capacity retention, reaching SOH 80% at 850 cycles, 550 cycles and 350 cycles, respectively. The pouch cell capacities and SOHs at certain number of cycles are collected in Supporting information, Table S1. Based on these results, the lithiation-step Mg-doping seems to enhance the cyclability of both stoichiometric and over-lithiated LCOs. Especially the lithiation step doping enhances the over-lithiated LCO. On the other hand, the precursor doping seems to worsen the cyclability of the LCO regardless the amount of lithium in the compound. The poor capacity retention of s-P-LCO is slightly unexpected, as the rate capability measurements in Fig. 3c suggest similar behavior to s-L-LCO. The difference might be caused by the small amount of  $\text{Co}_3\text{O}_4$  observed in the Raman measurements (Fig. 1c).  $\text{Co}_3\text{O}_4$  is not conductive and it could obstruct Li-ion diffusion in the material leading to poorer capacity retention. To understand the cycling behavior of the LCO materials, the differential capacity plotted against voltage is presented in Fig. S6. In the plots the main delithiation peak is observed to move towards higher voltages and the lithiation peak to lower voltages upon cycling which indicates increasing polarization of the electrodes with the increasing cycle number [50]. This matter will be discussed more in the EIS results section.

A typical set of XANES data from pouch cells measured at different SOC is shown in Fig. 4. The spectra consist of a pre-edge at 7.709 keV, after which the spectral weight increases until a peak called the main edge is reached at  $\sim 7.73$  keV. When the SOC increases, the oxidation state of Co increases, which is seen as changes in the spectra, most importantly as the increase of the energy position of the main edge. Upon discharge, the process reverses and Co oxidation state decreases, which makes the main edge position to decrease on the energy axis. The aging of the pouch cells can be observed to decrease the difference between SOC 0% and 100%, and the change in oxidation state is expected to be proportional to the change in the peak position's energy.

Thus, to investigate the oxidation state of the Co in the positive electrode of the pouch cells in more detail, the derivatives of the XANES spectra (Fig. 4) are presented in Fig. 5. The oxidation states were obtained by determining the zero crossing of the XANES spectra derivatives. The spectra of  $\text{CoO}$  and  $\text{LiCoO}_2$  were used as references for  $\text{Co}^{2+}$  and  $\text{Co}^{3+}$ , respectively. The change in the zero crossing energy position as a function of Co oxidation state was assumed to be linear, which allowed the determination of the sample oxidation states and the extrapolation of the zero crossing for  $\text{Co}^{4+}$ . It should be noted that the oxidation state value determined in this way may exceed 4.0, within the mentioned assumptions. Because of the discreteness of the spectral data point grid in the energy axis, and the statistical noise, cubic spline

smoothing was used to interpolate the experimental derivative curves to obtain the estimated position of the zero crossing. The reliability of the smoothing was checked carefully manually for each individual curve in order to confirm the accuracy of the extracted oxidation state values. The obtained Co valences are presented in Fig. 6 as the function of specific capacity. It is observed that the Co oxidation states in all the cells exceed that of the powder reference  $\text{LiCoO}_2$ , being  $+3.4$  on average for formatted cells. The increase in the oxidation state is most likely caused by the formation of the cells, which was done before the investigation. The irreversible reactions, such as formation of SEI layer on the graphite electrode [53,54], lead to Li loss and thus to the increase of the Co oxidation state. When the cell is charged, the oxidation state increases with the maximum value depending on the sample. For formatted cells, s-P-LCO reaches the highest value,  $+4.1$ , while o-P-LCO the lowest,  $+3.8$ . The other samples reach values between these two, with the stoichiometric samples having higher maximum values compared to the over-lithiated ones. Interestingly, this result is similar with the rate capability results presented in Fig. 3c which show better capability for the stoichiometric samples than for the over-lithiated samples. Previously Shibuya et al. have showed that  $\text{Li}_x\text{CoO}_2$  becomes more electrically conductive with decreasing  $x$  and increasing Co valence [55]. Our results therefore indicate that higher maximum oxidation state improves the conductivity and thus the rate capability.

When the cells are aged, the highest reachable oxidation state decreases. However, contradictory to our original hypothesis, the drop in the maximum reachable oxidation state does not correlate with the capacity retention. Instead, the difference in the Co valence between the discharged and charged states during one cycle, and the decrease of this difference upon cycling is observed to reflect the aging. For s-L-LCO, o-L-LCO and s-LCO, which showed the best capacity retention during the cycling (Fig. 3d), the differences are similar, approximately 0.55 at the beginning of the cycling and 0.45–0.48 at the end. However, for s-P-LCO and o-P-LCO, which have the poorest capacity retentions, these values are 0.63 and 0.64 at the beginning and 0.39 and 0.30 at the end. Therefore, the oxidation state of the precursor-doped samples varies more at the beginning of the cycling, but the range decrease faster than for the non-doped and lithiation-doped samples.

Based on the results above, it is concluded that the doping method affects the valence state of the LCOs during cycling. This is surprising, as the amount of Mg in the lithiation-doped and precursor-doped samples is similar, and the change in Co valence caused by the smaller valence of  $\text{Mg}^{2+}$  could be expected to be similar for both. However, due to the small amount of dopants in the samples, it is quite likely that the charge compensation of Co is not actually visible in the XANES data but instead, the effects of the dopants and doping methods are. The lithiation-doped LCOs have Mg evenly distributed in the lattice and smaller primary particle size, and these alone can lead to better charge transfer and Li-ion diffusion in the material leading to enhanced performance, e.g. stabilizing the structure, and to less irreversible phase changes. The worse performing materials have higher polarization, which can be linked to irreversible phase that can decrease the Co oxidation state range.

To understand the behavior behind the cyclability of the materials better, EIS was measured in both pouch cells and three-electrode set-up at the SoC of 50%. The complex-plane plots of the former are presented in Fig. 7 and the three-electrode cell plots in Supporting information Fig. S7. The complex-plane plots of the pouch cells show three semicircles at high and middle frequencies and a straight line at low frequencies. The high-frequency semicircle is attributed to the active material-current collector interface, the

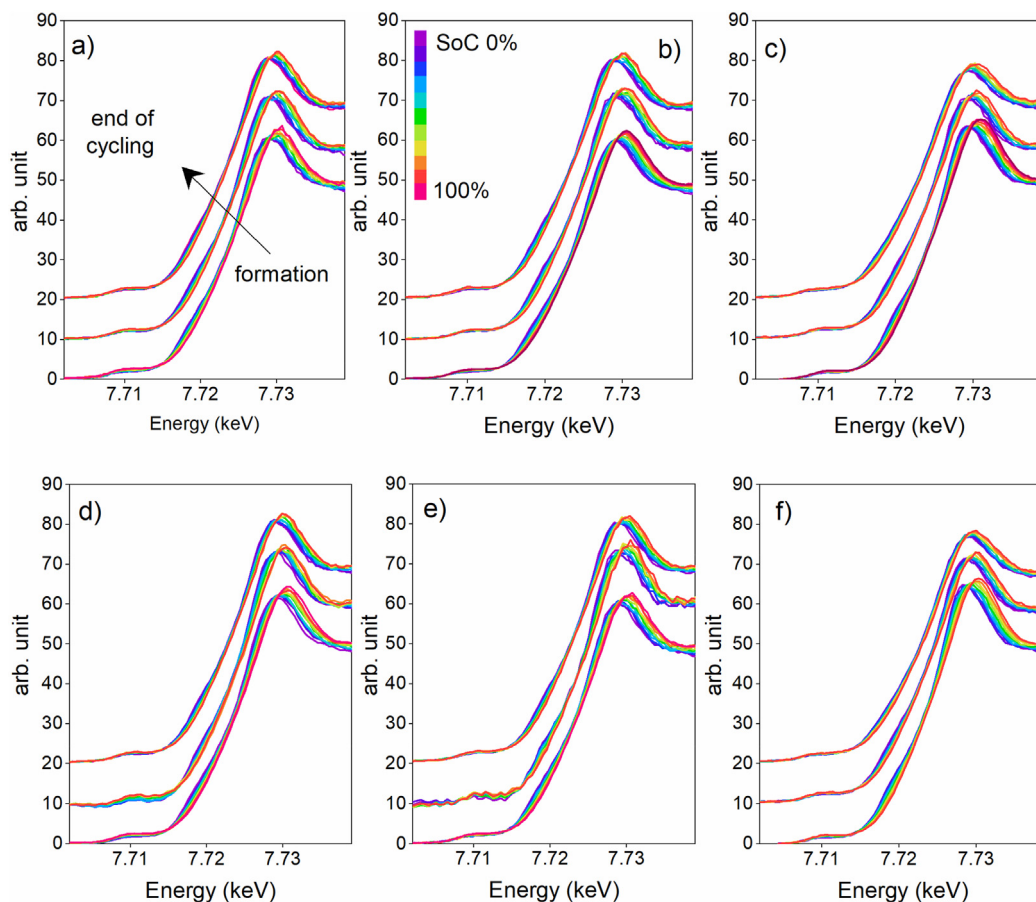


**Fig. 4.** Evolution of the pouch cells' XANES spectra upon aging. a) s-LCO, b) s-L-LCO, c) s-P-LCO, d) o-LCO, e) o-L-LCO and f) o-P-LCO.

midmost frequency semicircle to the charge transfer resistance of the negative electrode, the low-frequency semicircle to the charge transfer resistance of the positive electrode, and the low-frequency line to the solid-phase diffusion [56,57]. In the complex-plane plots of the three-electrode cells, two semicircles are observed instead of three. The results are interpreted similarly to the pouch cells, and the one middle-frequency semicircle is attributed to the charge-transfer resistance of the investigated LCOs.

The kinetic parameters based on the equivalent circuits of the pouch cell data are collected in Table 4 and those for the three-electrode set-up in Table S2. The equivalent series resistance ( $R_S$ ) is observed to increase slightly for the latter upon cycling. The resistance results mostly from ionic conduction in the separator-electrolyte phase of the cells and the electric conduction in the electrodes and current collectors. The increase indicates that the ionic conductivity of the electrolyte decreases upon cycling and can be ascribed to the degradation of the electrolyte on the surface of the metallic Li counter electrode. The equivalent series resistance in the pouch cells stays relatively similar upon cycling. The small changes are attributed to variations in the cell set-ups.

The high-frequency semicircle (active material/current collector interface resistance,  $R_I$ ) increases in the pouch cells upon cycling. The initial values vary between 0.07  $\Omega$  and 0.18  $\Omega$  for all materials except for o-P-LCO, for which the initial resistance is 0.27  $\Omega$ . After the cycling the resistance increases typically with 0.20–0.25  $\Omega$ . There are no notable differences between the materials. The increasing interface resistance indicates that contact between the particles and the current collector worsens with cycling. This could

be caused by the loss of the particle contacts caused by volume changes during charge and discharge or formation of surface layers, such as solid electrolyte interphase (SEI) layer on the graphite particles. The second semicircle ( $R_N$ ) is attributed to the charge-transfer resistance of the negative electrode. It overlaps strongly with the third semicircle attributed to the charge-transfer resistance of the positive electrode ( $R_P$ ) and therefore it is difficult to analyze. However, the sum of  $R_P$  and  $R_N$  charge transfer resistances in the pouch cells is in agreement with the three-electrode measurements presented in Supporting information, and based on this, the EIS analysis of the pouch cells focuses on the positive electrode.

The clearest differences in the impedance data are observed in the charge-transfer resistances of the positive electrode. The charge-transfer resistances of s-LCO, s-L-LCO and s-P-LCO are 0.67  $\Omega$ , 0.32  $\Omega$  and 2.48  $\Omega$ , respectively, meaning that the charge-transfer resistance of s-P-LCO is much larger than that of s-LCO and s-L-LCO. For the over-lithiated materials, the initial charge-transfer resistances are 0.66  $\Omega$ , 0.28  $\Omega$  and 1.01  $\Omega$  for o-LCO, o-L-LCO and o-P-LCO, respectively. The values are similar with the stoichiometric materials with the same doping method except for o-P-LCO that has a smaller charge-transfer resistance than s-P-LCO. The large initial charge-transfer resistance is most likely caused by the small amount of  $\text{Co}_3\text{O}_4$  observed in the Raman measurements (Fig. 1c).  $\text{Co}_3\text{O}_4$  is not conductive and its presence in the s-P-LCO surface could hinder the charge transfer during the electrochemical reaction. In o-P-LCO, the over-lithiation might compensate the resistance increased by the precursor doping, and thus decrease the resistance.

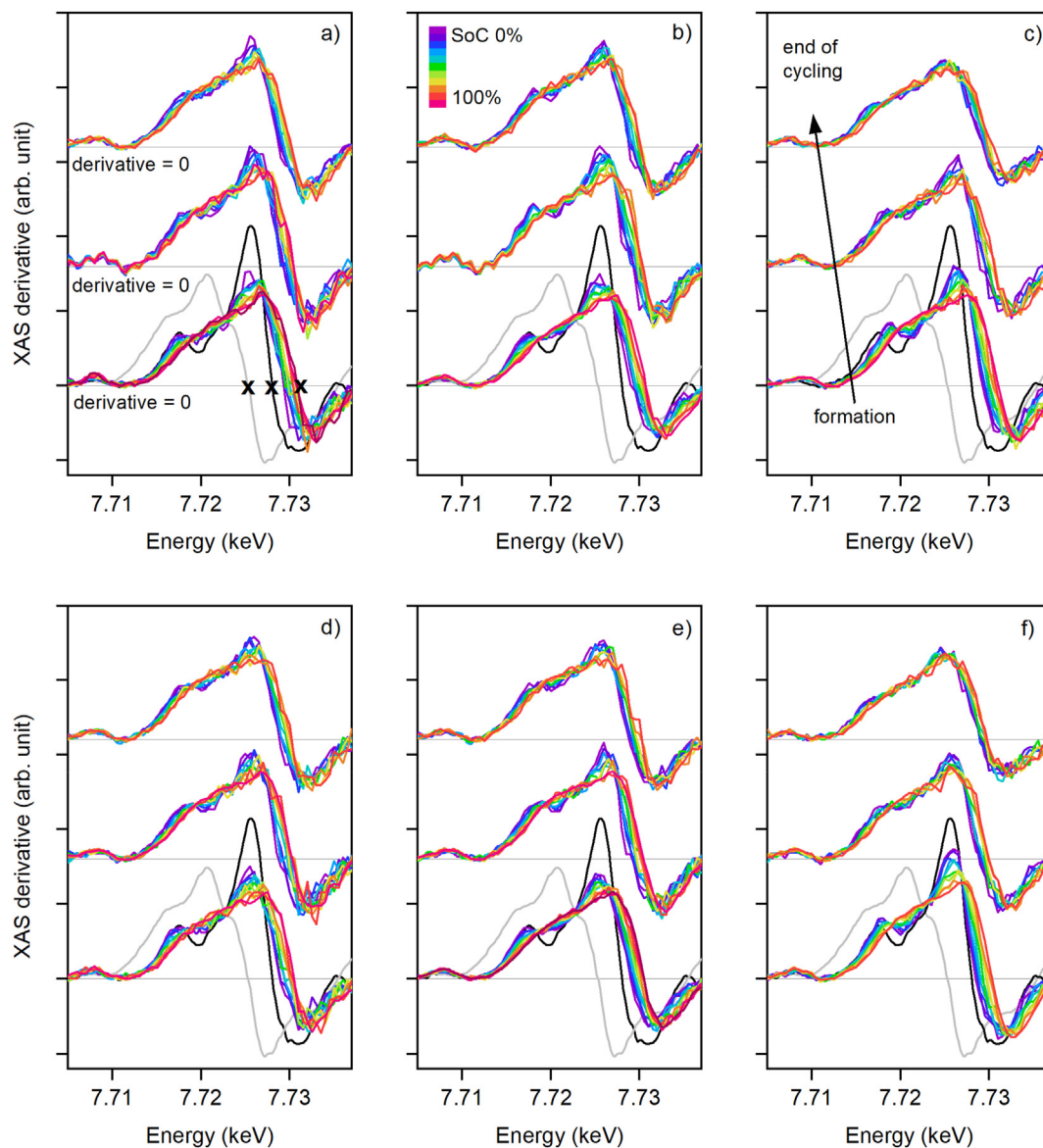


**Fig. 5.** Derivatives of the pouch cells' XANES spectra during cycling. a) s-LCO, b) s-L-LCO, c) s-P-LCO, d) o-LCO, e) o-L-LCO and f) o-P-LCO. The investigated materials are compared to two reference materials, CoO (grey line) and LiCoO<sub>2</sub> (black line) to determine the valence of the samples at each SoC. The three X-marks in figure a) present the energies corresponding to valences +2, +3 and +4, from left to right.

After the pouch cells are cycled, the increase in the charge-transfer resistance of s-L-LCO is the smallest, being now 0.77  $\Omega$ . The next smallest are o-L-LCO, s-LCO and o-LCO with 0.90  $\Omega$ , 1.33  $\Omega$  and 1.89  $\Omega$ , respectively. These results agree with the capacity retention data presented in Fig. 3d, in which the s-L-LCO is observed to have the best capacity retention. The charge-transfer resistance of s-P-LCO is the largest also after the cycling, being 3.01  $\Omega$ . However, the charge-transfer resistance of o-P-LCO has increased the most, being now 2.56  $\Omega$ . This reflects well the poorest capacity retention and lowest Co valence state range of o-P-LCO observed in Figs. 3d and 6, respectively. While the initial charge-transfer resistance of s-P-LCO is poorer than that of o-P-LCO, it increases less, and this most likely explains its better capacity retention. The results indicate that lithiation step Mg doping successfully reduces changes in the charge-transfer resistance of both stoichiometric and over-lithiated LCO. The

precursor Mg-doping, on the other hand, increases the charge-transfer resistance. In previous literature, LCO aging has been attributed to oxygen release accompanied by Co<sub>3</sub>O<sub>4</sub> formation, poor reversibility of high-voltage phase changes and passivation layer formation due to electrolyte decomposition at the particle surfaces [18,58–61]. Generally, the structural stability can be improved with doping, while passivation layer formation is prevented with coatings. The dopants do not affect the surface layer formation significantly [18,62]. Based on the XPS results in this study, the Mg/Co ratio on the lithiation-doped particle surfaces is smaller. This indicates that Mg has been more evenly distributed to the particles in lithiation-doped than precursor-doped LCOs. As the dopants do not affect the side reactions on the surfaces but the structural stability, the Mg in lithiation-doped samples is concluded to be so that it hinders more efficiently the structural changes, and this could explain the better capacity retention and

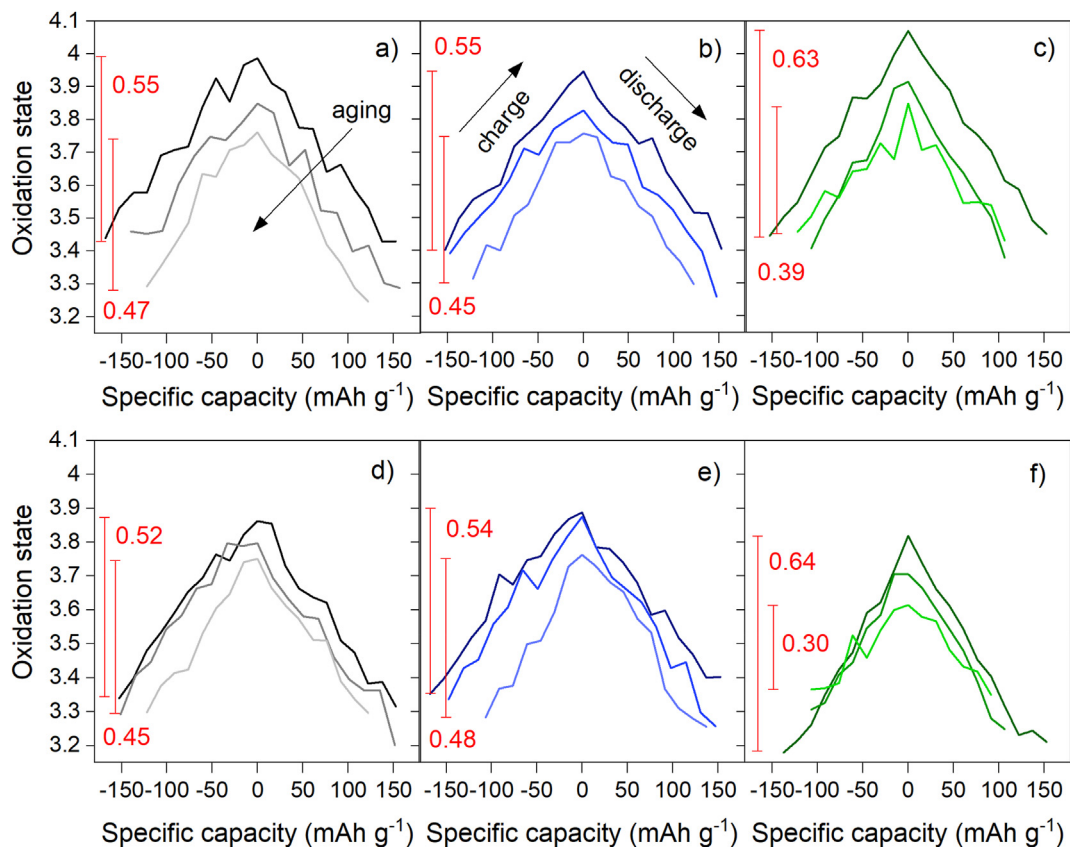


**Fig. 6.** Oxidation states of Co on the positive electrode of the LCO/graphite pouch cells determined based on the derivatives of the XANES spectra. a) s-LCO, b) s-L-LCO, c) s-P-LCO, d) o-LCO, e) o-L-LCO, f) o-P-LCO. The difference between minimum and maximum Co oxidation states at the beginning and the end of cycling are marked in the images with red lines.

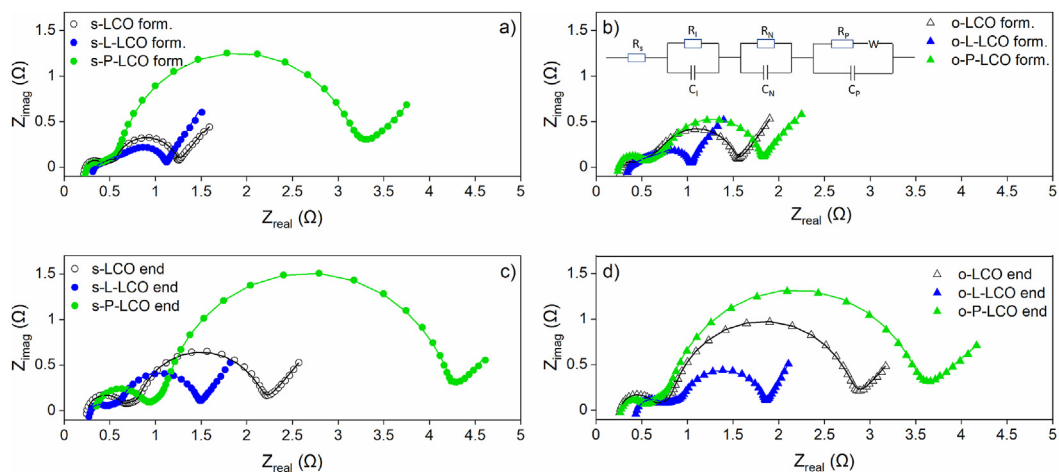


**Fig. 7.** Nyquist diagrams of the investigated LCOs in LCO/graphite pouch cells at SoC of 50% cycled in the voltage range of 3.0–4.3 V. a) Stoichiometric LCOs after formation, b) over-lithiated LCOs after formation, c) stoichiometric LCOs after cycling, d) over-lithiated LCOs after cycling. Experimental data is presented as dots and fitted data based on equivalent circuit as lines.

smaller charge-transfer resistance of the lithiation-doped LCOs. Mg has also previously been shown to enhance LCO conductivity [52], and its even distribution in the lattice can therefore enhance the charge-transfer as well.

It is also observed that for the non-doped materials, the charge-transfer resistance is larger for the over-lithiated than

stoichiometric material. This indicates that something in the over-lithiated material hinders the charge transfer. The XRD (Fig. 1 and Table 2) results show that the stacking order is poorer for the over-lithiated material than for the stoichiometric, and the more poorly ordered structure could hinder the charge transfer in the over-lithiated material seen as an increased semicircle.

**Table 4**  
Kinetic parameters of the pouch cells based on the equivalent circuit presented in Fig. 7.

	$R_S$ ( $\Omega$ )	$R_I$ ( $\Omega$ )	$R_N$ ( $\Omega$ )	$R_P$ ( $\Omega$ )
s-LCO form.	0.24	0.18	0.15	0.67
s-LCO end of cycling	0.25	0.39	0.18	1.33
s-L-LCO form.	0.34	0.04	0.35	0.38
s-L-LCO end of cycling	0.29	0.14	0.26	0.77
s-P-LCO form.	0.27	0.10	0.30	2.48
s-P-LCO end of cycling	0.34	0.48	0.35	3.01
o-LCO form.	0.29	0.10	0.48	0.66
o-LCO end of cycling	0.26	0.34	0.30	1.89
o-L-LCO form.	0.37	0.07	0.30	0.28
o-L-LCO end of cycling	0.45	0.29	0.19	0.90
o-P-LCO form.	0.25	0.27	0.25	1.01
o-P-LCO end of cycling	0.27	0.21	0.48	2.56

#### 4. Conclusion

In this work, more even Mg distribution in the lattice and smaller primary particle size are observed to induce smaller charge transfer resistance which is reflected as better rate capability and capacity retention. Stacking order determined from the XRD results is observed to affect electrochemical performance as well, the better stacking order resulting in better electrochemical performance. In the XANES results, the Co valence is observed to change during a charge-discharge cycle, the difference between the maximum and minimum valence of one cycle decreasing when the material is cycled. The decrease is smaller for the materials with a good capacity retention and low charge transfer resistance, which indicates that it is most likely caused by irreversible phase changes occurring in the material, and part of the LCO becoming electrochemically inactive.

In the synthesis conditions used in this study, the favorable Mg distribution and stacking order are achieved better with lithiation doping. This is reflected especially in the capacity and the Co valence state difference decreases, which are considerably poorer for the precursor doped LCO. Over-lithiation is observed to have an unfavorable effect on the stacking order compared to the stoichiometric lithiation, with the over-lithiated, lithiation-doped LCO as an exception.

#### Authors' contributions

**K. Lahtinen:** Conceptualization, Formal analysis, Investigation, Writing – original draft, Writing – review & editing, Visualization. **M. Labmayr:** Methodology, Investigation. **V. Mäkelä:** Methodology, Investigation. **H. Jiang:** Investigation, Writing – review & editing. **J. Lahtinen:** Investigation, Formal analysis, Writing – review & editing. **L. Yao:** Investigation. **E. O. Fedorovskaya:** Writing – review & editing. **S. Räsänen:** Conceptualization, Resources, Writing – review & editing. **S. Huotari:** Methodology, Formal analysis, Resources, Writing – review & editing, Funding. **T. Kallio:** Conceptualization, Writing – review & editing, Project administration, Funding.

#### Link to data

<https://etsin.fairdata.fi/dataset/0e8403db-c212-42a8-9b07-1c106247f84d/data>.

#### Declaration of competing interest

The authors declare that they have no known competing financial interests or personal relationships that could have appeared to influence the work reported in this paper.

#### Acknowledgements

This work made use of the Aalto University Otanano and RAMI infrastructures. The authors thank Dr. Eeva-Leena Rautama for the instruction and help with the modelling of XRD data. The authors also thank Dr. Juho Välikangas and Mr. Tuomo Vähätiitto from University of Oulu for optimizing and preparing the pouch cells. We acknowledge the University of Helsinki Center for X-ray Spectroscopy for providing the XANES experiments with the Hel-XAS spectrometer under Proposal number 2021–0007. Financial support from Academy of Finland (Strategic Research Council, the Profi 5 project) and the Grant No. 295696, and Business Finland (the BatCircle project No 2117574) is also greatly acknowledged.

#### Appendix A. Supplementary data

Supplementary data to this article can be found online at <https://doi.org/10.1016/j.mtener.2022.101040>.

#### References

- [1] Global Battery Alliance & World Economic Forum, A Vision for a Sustainable Battery Value Chain in 2030 Unlocking the Full Potential to Power Sustainable Development and Climate Change Mitigation, 2019.
- [2] J. Bobba, S. Carrara, J. Huisman, F. Mathieux, C. Pavel, Critical Raw Materials for Strategic Technologies and Sectors in the EU A Foresight Study by European Commission, 2020, <https://doi.org/10.2873/58081>.
- [3] D.J. Garole, R. Hossain, V.J. Garole, V. Sahajwalla, J. Nerkar, D.P. Dubal, Recycle, recover and repurpose strategy of spent Li-ion batteries and catalysts: current status and future opportunities, *ChemSusChem* 13 (2020) 3079–3100, <https://doi.org/10.1002/cssc.201903213>.
- [4] J.W. Fergus, Recent developments in cathode materials for lithium ion batteries, *J. Power Sources* 195 (2010) 939–954, <https://doi.org/10.1016/j.jpowsour.2009.08.089>.
- [5] M.R. Laskar, D.H.K. Jackson, S. Xu, R.J. Hamers, D. Morgan, T.F. Kuech, Atomic layer deposited MgO: a lower overpotential coating for Li[Ni<sub>0.5</sub>Mn<sub>0.3</sub>Co<sub>0.2</sub>]O<sub>2</sub> cathode, *ACS Appl. Mater. Interfaces* 9 (2017) 11231–11239, <https://doi.org/10.1021/acsami.6b16562>.
- [6] S. Sharifi-Asl, J. Lu, K. Amine, R. Shahbazian-Yassar, Oxygen release degradation in Li-ion battery cathode materials: mechanisms and mitigating approaches, *Adv. Energy Mater.* 9 (2019), <https://doi.org/10.1002/aenm.201900551>.
- [7] F. Nobili, F. Croce, R. Tossici, I. Meschini, P. Reale, R. Marassi, Sol-gel synthesis and electrochemical characterization of Mg-Zr-doped LiCoO<sub>2</sub> cathodes for Li-ion batteries, *J. Power Sources* 197 (2012) 276–284, <https://doi.org/10.1016/j.jpowsour.2011.09.053>.
- [8] C. Julien, G.A. Nazri, A. Rougier, Electrochemical performances of layered LiM<sub>1</sub>-yM<sub>2</sub>yO<sub>2</sub> (M=Ni, Co; M'=Mg, Al, B) oxides in lithium batteries, *Solid State Ionics* 135 (2000) 121–130.
- [9] Y. Huang, Y. Zhu, H. Fu, M. Ou, C. Hu, S. Yu, Z. Hu, C. Te Chen, G. Jiang, H. Gu, H. Lin, W. Luo, Y. Huang, Mg-pillared LiCoO<sub>2</sub>: towards stable cycling at 4.6 V, *Angew. Chem. Int. Ed.* 60 (2021) 4682–4688, <https://doi.org/10.1002/anie.202014226>.
- [10] L. Xu, K. Wang, F. Gu, T. Li, Z. Wang, Determining the intrinsic role of Mg doping in LiCoO<sub>2</sub>, *Mater. Lett.* 277 (2020) 1–4, <https://doi.org/10.1016/j.matlet.2020.128407>.
- [11] J. Yu, Z. Han, X. Hu, H. Zhan, Y. Zhou, X. Liu, The investigation of Ti-modified LiCoO<sub>2</sub> materials for lithium ion battery, *J. Power Sources* 262 (2014) 136–139, <https://doi.org/10.1016/j.jpowsour.2014.03.073>.
- [12] A. Liu, J. Li, R. Shunmugasundaram, J.R. Dahn, Synthesis of Mg and Mn doped LiCoO<sub>2</sub> and effects on high voltage cycling, *J. Electrochem. Soc.* 164 (2017) A1655–A1664, <https://doi.org/10.1149/2.1381707jes>.
- [13] W. Kong, D. Zhou, De Ning, W. Yang, D. Wong, J. Zhang, Q. Li, J. Yang, C. Schulz, X. Liu, Unraveling the distinct roles of Mg occupation on Li or Co sites on high-voltage LiCoO<sub>2</sub>, *J. Electrochem. Soc.* 168 (2021), 030528, <https://doi.org/10.1149/1945-7111/abebf7>.
- [14] S. Mou, K. Huang, M. Guan, X. Ma, J. song Chen, Y. Xiang, X. Zhang, Reduced energy barrier for Li<sup>+</sup> diffusion in LiCoO<sub>2</sub> via dual doping of Ba and Ga, *J. Power Sources* 505 (2021) 230067, <https://doi.org/10.1016/j.jpowsour.2021.230067>.
- [15] S.H. Ju, H.C. Jang, Y.C. Kang, LiCo<sub>1-x</sub>Al<sub>x</sub>O<sub>2</sub> (0 ≤ x ≤ 0.05) cathode powders prepared from the nanosized Co<sub>1-x</sub>Al<sub>x</sub>O<sub>y</sub> precursor powders, *Mater. Chem. Phys.* 112 (2008) 536–541, <https://doi.org/10.1016/j.matchemphys.2008.06.011>.
- [16] Y.S. Hong, X. Huang, C. Wei, J. Wang, J.N. Zhang, H. Yan, Y.S. Chu, P. Pianetta, R. Xiao, X. Yu, Y. Liu, H. Li, Hierarchical defect engineering for LiCoO<sub>2</sub> through low-solubility trace element doping, *Inside Chem.* 6 (2020) 2759–2769, <https://doi.org/10.1016/j.chempr.2020.07.017>.

- [17] Y. Wang, T. Cheng, Z.E. Yu, Y. Lyu, B. Guo, Study on the effect of Ni and Mn doping on the structural evolution of LiCoO<sub>2</sub> under 4.6 V high-voltage cycling, *J. Alloys Compd.* 842 (2020) 155827, <https://doi.org/10.1016/j.jallcom.2020.155827>.
- [18] A. Fu, Z. Zhang, J. Lin, Y. Zou, C. Qin, C. Xu, P. Yan, K. Zhou, J. Hao, X. Yang, Y. Cheng, D.Y. Wu, Y. Yang, M.S. Wang, J. Zheng, Highly stable operation of LiCoO<sub>2</sub> at cut-off  $\geq$  4.6 V enabled by synergistic structural and interfacial manipulation, *Energy Storage Mater.* 46 (2022) 406–416, <https://doi.org/10.1016/j.ensm.2022.01.033>.
- [19] S. Song, B. Peng, X. Peng, X. Zhang, Y. Xiang, Improving the cycling stability of LiCoO<sub>2</sub> at 4.5 V by Mg doping and graphite coating, *IOP Conf. Ser. Earth Environ. Sci.* 526 (2020), <https://doi.org/10.1088/1755-1315/526/1/012082>.
- [20] S. Levasseur, M. Menetrier, Y. Shao-Horn, L. Gautier, A. Audemer, G. Demazeau, A. Largeau, C. Delmas, Oxygen vacancies and intermediate spin trivalent cobalt ions in lithium-overstoichiometric LiCoO<sub>2</sub>, *Chem. Mater.* 15 (2003) 348–354, <https://doi.org/10.1021/cm021279g>.
- [21] N. Imanishi, M. Fujii, A. Hirano, Y. Takeda, Synthesis and characterization of nonstoichiometric LiCoO<sub>2</sub>, *J. Power Sources* 97–99 (2001) 287–289, [https://doi.org/10.1016/S0378-7753\(01\)00740-6](https://doi.org/10.1016/S0378-7753(01)00740-6).
- [22] P. Hovington, M. Dontigny, A. Guerfi, J. Trottier, M. Lagacé, A. Mauger, C.M. Julien, K. Zaghib, In situ Scanning electron microscope study and microstructural evolution of nano silicon anode for high energy Li-ion batteries, *J. Power Sources* 248 (2014) 457–464, <https://doi.org/10.1016/j.jpowsour.2013.09.069>.
- [23] Z. Wang, D. Santhanagopalan, W. Zhang, F. Wang, H.L. Xin, K. He, J. Li, N. Dudney, Y.S. Meng, In situ STEM-EELS observation of nanoscale interfacial phenomena in all-solid-state batteries, *Nano Lett.* 16 (2016) 3760–3767, <https://doi.org/10.1021/acs.nanolett.6b01119>.
- [24] L. Cai, K. An, Z. Feng, C. Liang, S.J. Harris, In-situ observation of inhomogeneous degradation in large format Li-ion cells by neutron diffraction, *J. Power Sources* 236 (2013) 163–168, <https://doi.org/10.1016/j.jpowsour.2013.02.066>.
- [25] P. Novák, J.C. Panitz, F. Joho, M. Lanz, R. Imhof, M. Coluccia, Advanced in situ methods for the characterization of practical electrodes in lithium-ion batteries, *J. Power Sources* 90 (2000) 52–58, [https://doi.org/10.1016/S0378-7753\(00\)00447-X](https://doi.org/10.1016/S0378-7753(00)00447-X).
- [26] Y. Orikasa, T. Maeda, Y. Koyama, H. Murayama, K. Fukuda, H. Tanida, H. Arai, E. Matsubara, Y. Uchimoto, Z. Ogumi, Direct observation of a metastable crystal phase of Li<sub>1-x</sub>FePO<sub>4</sub> under electrochemical phase transition, *J. Am. Chem. Soc.* 135 (2013) 5497–5500, <https://doi.org/10.1021/ja312527x>.
- [27] X. Liu, D. Wang, G. Liu, V. Srinivasan, Z. Liu, Z. Hussain, W. Yang, Distinct charge dynamics in battery electrodes revealed by in situ and operando soft X-ray spectroscopy, *Nat. Commun.* 4 (2013) 1–8, <https://doi.org/10.1038/ncomms3568>.
- [28] J. Wang, Y.C.K. Chen-Wiegart, J. Wang, In operando tracking phase transformation evolution of lithium ion phosphate with hard X-ray microscopy, *Nat. Commun.* 5 (2014) 1–10, <https://doi.org/10.1038/ncomms5570>.
- [29] S.M. Bak, Z. Shadike, R. Lin, X. Yu, X.Q. Yang, In situ/operando synchrotron-based X-ray techniques for lithium-ion battery research, *NPG Asia Mater.* 10 (2018) 563–580, <https://doi.org/10.1038/s41427-018-0056-z>.
- [30] P.P.R.M.L. Harks, F.M. Mulder, P.H.L. Notten, In situ methods for Li-ion battery research: a review of recent developments, *J. Power Sources* 288 (2015) 92–105, <https://doi.org/10.1016/j.jpowsour.2015.04.084>.
- [31] C. Van Bokhoven, Jeroen A. Lamberti, X-Ray Absorption and X-Ray Emission Spectroscopy, John Wiley & Sons, 2016, <https://doi.org/10.1002/9781118844243>.
- [32] Z. Németh, J. Szlachetko, É.G. Bajnóczi, G. Vankó, Laboratory von Hámos X-ray spectroscopy for routine sample characterization, *Rev. Sci. Instrum.* 87 (2016) 103105, <https://doi.org/10.1063/1.4964098>.
- [33] G.T. Seidler, D.R. Mortensen, A.J. Remesnik, J.I. Pacold, N.A. Ball, N. Barry, M. Stycziński, O.R. Hoidn, A laboratory-based hard x-ray monochromator for high-resolution x-ray emission spectroscopy and x-ray absorption near edge structure measurements, *Rev. Sci. Instrum.* 85 (2014) 113906, <https://doi.org/10.1063/1.4901599>.
- [34] A.P. Honkanen, S. Ollikkala, T. Ahopelto, A.J. Kallio, M. Blomberg, S. Huotari, Johann-type laboratory-scale x-ray absorption spectrometer with versatile detection modes, *Rev. Sci. Instrum.* 90 (2019), 033107, <https://doi.org/10.1063/1.5084049>.
- [35] A.S. Ditter, E.P. Jahrman, L.R. Bradshaw, X. Xia, P.J. Pauzauskie, G.T. Seidler, A mail-in and user facility for X-ray absorption near-edge structure: the CELEXANES laboratory X-ray spectrometer at the University of Washington, *J. Synchrotron Radiat.* 26 (2019) 2086–2093, <https://doi.org/10.1107/S1600577519012839>.
- [36] E.P. Jahrman, L.A. Pellerin, A.S. Ditter, L.R. Bradshaw, T.T. Fister, B.J. Polzin, S.E. Trask, A.R. Dunlop, G.T. Seidler, Laboratory-based X-ray absorption spectroscopy on a working pouch cell battery at industrially-relevant charging rates, *J. Electrochem. Soc.* 166 (2019) A2549–A2555, <https://doi.org/10.1149/2.0721912jes>.
- [37] M. Rovezzi, C. Lapras, A. Manceau, P. Glatzel, R. Verbeni, High energy-resolution x-ray spectroscopy at ultra-high dilution with spherically bent crystal analyzers of 0.5 m radius, *Rev. Sci. Instrum.* 88 (2017), <https://doi.org/10.1063/1.4974100>, 0–9.
- [38] J. Rodriguez-Carvajal, Recent advances in magnetic structure determination by neutron powder diffraction, *Phys. B Condens. Matter* 92 (1993) 55–69, [https://doi.org/10.1016/0921-4526\(93\)90108-I](https://doi.org/10.1016/0921-4526(93)90108-I).
- [39] R.D. Shannon, Revised effective ionic radii and systematic studies of interatomic distances in halides and chalcogenides, *Acta Crystallogr. A32* (1976) 751–767.
- [40] M. Mladenov, R. Stoyanova, E. Zheheva, S. Vassilev, Effect of Mg doping and MgO-surface modification on the cycling stability of LiCoO<sub>2</sub> electrodes, *Electrochem. Commun.* 3 (2001) 410–416, [https://doi.org/10.1016/S1388-2481\(01\)00192-8](https://doi.org/10.1016/S1388-2481(01)00192-8).
- [41] S. Sivaprakash, S.B. Majumder, S. Nieto, R.S. Katiyar, Crystal chemistry modification of lithium nickel cobalt oxide cathodes for lithium ion rechargeable batteries, *J. Power Sources* 170 (2007) 433–440, <https://doi.org/10.1016/j.jpowsour.2007.04.029>.
- [42] D.H. Pearson, C.C. Ahn, B. Fultz, White lines and d-electron occupancies for the 3d and 4d transition metals, *Phys. Rev. B* 47 (1993) 8471–8478.
- [43] Z.L. Wang, J.S. Yin, Y.D. Jiang, EELS analysis of cation valence states and oxygen vacancies in magnetic oxides, *Micron* 31 (2000) 571–580, [https://doi.org/10.1016/S0968-4328\(99\)00139-0](https://doi.org/10.1016/S0968-4328(99)00139-0).
- [44] M. Inaba, Y. Iriyama, Z. Ogumi, Y. Todzuka, A. Tasaka, Raman study of layered rock-salt LiCoO<sub>2</sub> and its electrochemical lithium deintercalation, *J. Raman Spectrosc.* 28 (1997) 613–617.
- [45] R. Baddour-Hadjean, J.-P. Pereira-Ramos, Raman microspectrometry applied to the study of electrode materials for lithium batteries, *Chem. Rev.* 110 (2010) 1278–1319, <https://doi.org/10.1021/cr800344k>.
- [46] R. Alcántara, G.F. Ortiz, P. Lavela, J.L. Tirado, W. Jaegermann, A. Thißen, Rotor blade grinding and re-annealing of LiCoO<sub>2</sub>: SEM, XPS, EIS and electrochemical study, *J. Electroanal. Chem.* 584 (2005) 147–156, <https://doi.org/10.1016/j.jelechem.2005.07.011>.
- [47] Y. Meng, G. Wang, M. Xiao, C. Duan, C. Wang, F. Zhu, Y. Zhang, Ionic liquid-derived Co<sub>3</sub>O<sub>4</sub>/carbon nano-onions composite and its enhanced performance as anode for lithium-ion batteries, *J. Mater. Sci.* 52 (2017) 13192–13202, <https://doi.org/10.1007/s10853-017-1414-x>.
- [48] M.C. Biesinger, B.P. Payne, A.P. Grosvenor, L.W.M. Lau, A.R. Gerson, R.S.C. Smart, Resolving surface chemical states in XPS analysis of first row transition metals, oxides and hydroxides: Cr, Mn, Fe, Co and Ni, *Appl. Surf. Sci.* 257 (2011) 2717–2730, <https://doi.org/10.1016/j.apsusc.2010.10.051>.
- [49] J.N. Reimers, J.R. Dahn, Electrochemical and in situ X-ray diffraction studies of lithium intercalation in LiCoO<sub>2</sub>, *J. Electrochem. Soc.* 139 (1992) 2091–2097, <https://doi.org/10.1149/1.2221184>.
- [50] P.T. Kissinger, W.R. Heineman, Cyclic voltammetry, *J. Chem. Educ.* 70 (1983) 702–706, <https://doi.org/10.1021/ed060p702>.
- [51] T. Kim, W. Choi, H.C. Shin, J.Y. Choi, J.M. Kim, M.S. Park, W.S. Yoon, Applications of voltammetry in lithium ion battery research, *J. Electrochem. Sci. Technol.* 11 (2020) 14–25, <https://doi.org/10.33961/jecst.2019.00619>.
- [52] H. Takamoto, A.R. West, Electronic conductivity of LiCoO<sub>2</sub> and its enhancement by magnesium doping, *J. Electrochem. Soc.* 144 (1997) 3164–3168, <https://doi.org/10.1149/1.1837976>.
- [53] R. Hausbrand, G. Cherkashinin, H. Ehrenberg, M. Gröting, K. Albe, C. Hess, W. Jaegermann, Fundamental degradation mechanisms of layered oxide Li-ion battery cathode materials: Technology, insights and novel approaches, *Mater. Sci. Eng. B Solid-State Mater. Adv. Technol.* 192 (2015) 3–25, <https://doi.org/10.1016/j.mseb.2014.11.014>.
- [54] K. Lahtinen, E.L. Rautama, H. Jiang, S. Räsänen, T. Kallio, Reuse of LiCoO<sub>2</sub> electrodes collected from spent Li-ion batteries after electrochemical Relithiation of the electrode, *ChemSusChem* 14 (2021) 2434–2444, <https://doi.org/10.1002/cssc.202100629>.
- [55] M. Shibuya, T. Nishina, T. Matsue, I. Uchida, In situ conductivity measurements of LiCoO<sub>2</sub> film during lithium insertion/extraction by using interdigitated microarray electrodes, *J. Electrochem. Soc.* 143 (1996) 3157–3160, <https://doi.org/10.1149/1.1837180>.
- [56] H. Zheng, G. Liu, X. Song, V. Battaglia, Li[Ni<sub>1/3</sub>Mn<sub>1/3</sub>Co<sub>1/3</sub>]O<sub>2</sub>-based electrodes for PHEV applications: an optimization, *ECS Trans* 11 (2008) 1–9, <https://doi.org/10.1149/1.2992488>.
- [57] Y.-C. Chang, H.-J. Sohn, Electrochemical impedance analysis for lithium ion intercalation into graphitized carbons, *J. Electrochem. Soc.* 147 (2000) 50, <https://doi.org/10.1149/1.1393156>.
- [58] X. Lu, Y. Sun, Z. Jian, X. He, L. Gu, Y.S. Hu, H. Li, Z. Wang, W. Chen, X. Duan, L. Chen, J. Maier, S. Tsukimoto, Y. Ikuhara, New insight into the atomic structure of electrochemically delithiated O<sub>3</sub>-Li(1-x)CoO<sub>2</sub> (0 ≤ x ≤ 0.5) nanoparticles, *Nano Lett.* 12 (2012) 6192–6197, <https://doi.org/10.1021/nl303036e>.
- [59] J. Zheng, M. Gu, J. Xiao, P. Zuo, C. Wang, J.G. Zhang, Corrosion/fragmentation of layered composite cathode and related capacity/voltage fading during cycling process, *Nano Lett.* 13 (2013) 3824–3830, <https://doi.org/10.1021/nl401849c>.
- [60] J. Zhang, Q. Li, C. Ouyang, X. Yu, M. Ge, X. Huang, E. Hu, C. Ma, S. Li, R. Xiao, W. Yang, Y. Chu, Y. Liu, H. Yu, X. Yang, X. Huang, L. Chen, H. Li, Trace doping of multiple elements enables stable battery cycling of LiCoO<sub>2</sub> at 4.6 V, *Nat. Energy* 4 (2019) 594–603, <https://doi.org/10.1038/s41560-019-0409-z>.
- [61] A. Yano, M. Shikano, A. Ueda, H. Sakaebe, Z. Ogumi, LiCoO<sub>2</sub> degradation behavior in the high-voltage phase transition region and improved reversibility with surface coating, *J. Electrochem. Soc.* 164 (2017) A6116–A6122, <https://doi.org/10.1149/2.0181701jes>.
- [62] P. Zhang, C. Xie, G. Han, Q. Zhu, L. Chen, M. Jin, Q. Liu, Y. Zhou, Q. Sun, J. Xie, Stable cycling of LiCoO<sub>2</sub> at 4.55 V enabled by combined Mg doping and surface coating of NASICON-type electrolyte, *Mater. Today Nano* 15 (2021) 100122, <https://doi.org/10.1016/j.mtnano.2021.100122>.



**Katja Lahtinen**, M.Sc.(Tech.), is a doctoral student in Aalto University, School of Chemical Engineering, Research group of Electrochemical Energy Conversion. Her doctoral studies have focused on understanding the electrode materials in Li-ion batteries. The public examination of her doctoral dissertation takes place in April 2022, the topic being "Cycle Life and Recycling of Positive Electrode Materials in Li-Ion Batteries".



**Dr. Lide Yao** is a staff scientist at OtaNano-Nanoscience Center of Aalto University (Finland) since 2019. He received a PhD in condensed matter physics from the Institute of Physics, Chinese Academy of Sciences (China) in 2008. His current research interest is mainly focusing on developing and utilizing advanced ion milling technique and in-situ transmission electron microscopy for innovative studies on electrically and thermally driven nanoscale functional materials.



**Maximilian Labmayr**, M.Sc., is a physicist who specialized in energy engineering. During his Master's degree he joined the research group of Electrochemical Energy Conversion at Aalto University and conducted experiments on cathode materials for Li-ion batteries. He is currently working as a management consultant in the energy sector.



**Dr. Ekaterina Fedorovskaya** have been doing scientific research since 2003. During this time, Dr. Ekaterina Fedorovskaya was working with synthesis, functionalization, characterization and electrochemical tests of graphene materials, carbon nanotubes, conductive polymers, transition metal oxides/hydroxides, lithiated transition metal oxides for supercapacitor, biosensors, and Li-ion battery applications. Nowadays Ekaterina is working as associate professor in School of Engineering Science of LUT University developing infrastructure for the Li battery research and continuing study and teaching related to materials for the electrochemical energy storage and material recycling.



**Dr. Hua Jiang** is a Senior Scientist in Nanoscience Center of Aalto University. He earned his PhD degree in science from Beijing Institute of Physics (IOP), Chinese Academy of Sciences. He has been working in the field of advanced electron microscopy and its applications in materials science, especially in nano-carbon materials over the last decades.



**Prof. Simo Huotari**, Ph.D., is a professor in experimental materials physics. He is the Head of the Department of Physics of the University of Helsinki, Finland, since 2021 and leader of the X-ray physics research group at the University of Helsinki since 2015. He received his PhD in 2003 at the University of Helsinki, after which he worked at the European Synchrotron Radiation Facility until 2010 after which he returned to the University of Helsinki. His has specialized in developing and using novel x-ray analytical methods, including x-ray spectroscopy and inelastic x-ray scattering, in materials physics and chemistry.



**Dr. Jouko Lahtinen** received his D.Sc.(Eng.) degree in Engineering Physics in 1991 from the Helsinki University of Technology. He has supervised the Surface Science Group at Helsinki University of Technology and Aalto University, Finland after returning from UC Berkeley in 1992. He is a specialist in X-Ray Photoelectron Spectroscopy and catalyst surface studies.



**Prof. Tanja Kallio**, D.Sc.(Eng.), has been heading the Electrochemical Energy Conversion Team at the Aalto University (Finland) since 2015. She received a D.Sc.(Eng.) degree on Physical Chemistry and Electrochemistry from the Helsinki University of Technology in the year 2003. Tanja Kallio's research focuses on investigation and development of materials for electrochemical energy conversion and storage devices including polymer electrolyte fuel cells and electrolyzers, and lithium batteries. The core theme is more efficient utilization of non-earth-abundant elements without sacrificing the performance.